International Journal of Hydrogen Energy 95 (2024) 1126–1136

Contents lists available at ScienceDirect

International Journal of Hydrogen Energy

journal homepage: www.elsevier.com/locate/he

An experimentally derived calibration model for hydrogen-fueled solid oxide fuel cells at intermediate temperature

Zahreddine Hafsi *, Sebastian Vecino-Mantilla, Massimiliano Lo Faro

Institute for Advanced Energy Technologies (ITAE) of the National Research Council of Italy (CNR), Via Salita S. Lucia Sopra Contesse 5, 98126, Messina, Italy

ARTICLE INFO

Handling Editor: Ibrahim Dincer

Keywords:
Green deal
Gas-to-power
Analytical development
Experimental fitting
Renewable
REPowerEU

ABSTRACT

The characteristic polarization curve (e.g. I–V curve) of a solid oxide fuel cell (SOFC) is a valuable outcome of experimental tests because it conveys crucial information about the SOFC's current-potential operational range and optimum performance point. Numerical analysis of the experimentally achieved I–V curve can yield information that is not readily available from it, such as parameters of operation, kinetics of electrochemical reactions, and mechanisms of mass and current transfer. Such details can be used to choose optimal operating conditions and improve the cell manufacturing process. Using experimental polarization curves of a commercial SOFC fed with hydrogen and air, this paper develops a calibration algorithm and extends the analysis to evaluate further operational parameters of the cell. The calibrated model was developed for a commercial SOFC operating at 700 °C and 800 °C. As target parameters, the calibrated model defined the anode and cathode exchange current densities as well as the effective diffusion coefficients of gas species within both electrodes and their respective pore radii. A comprehensive SOFC analysis model requires a detailed understanding of the morphology of the porous material inside the cell, and these parameters provided that insight. Using experimental and analytically optimized polarization curves, target parameters are defined with an accuracy of more than 98%. Based on the developed model, it was also possible to predict the maximum current density the cell could reach at temperatures of 800 °C and 700 °C, which was about 2 Acm^{-2} and 1.7 Acm^{-2}, respectively. Compared with SOFC parameters reported in literature, the obtained values were fully consistent. In spite of this, the algorithm outcomes are considered "equivalent" parameters since they are solutions to a multivariable problem, and only their combination with other known parameters can result in fitting a benchmark curve. Additionally, their uniqueness criterion is not yet investigated as a means of describing actual cell parameters.

1. Introduction

Solid oxide fuel cells (SOFCs) are a relatively recent concept that can be traced back to the second half of the 20th century [1]. Boosted by technological progress that allowed for reducing the working temperature of SOFCs while maintaining their efficiency and enhancing their durability [2–4], today, SOFCs are gaining increasing interest and are expected to become a cornerstone of decarbonized energy systems to advance the implementation of "green" industry practices [5]. The ability to predict SOFCs performance is a key aspect of integrating them into industrial processes in a circular economy context towards achieving the net zero carbon goal set by several industrialized countries to be reached in the decade between 2050 and 2060 [6–9].

Added to being a promising technology for clean energy production, from an economical point of view SOFCs are foreseen to be a major contributor to the global energy market. It has been widely reported that the overall efficiency of SOFC technology could reach up to 60%, a value high enough to consider SOFC as an advantageous technology outcompeting most existing power generation systems [10,11]. Furthermore, several research works have also evaluated the installation costs and payback periods of SOFC-based energy systems to gauge their cost-effectiveness. Some early studies have predicted SOFCs to be widely used in the near future based on a techno-economic analysis of their integration into the energy market. Indeed, Ippommatsu et al. [12], who expected SOFCs to be practical on the market, conducted a performance evaluation of the manufacturing cost of various single cells to check whether SOFCs could compete once this technology is widely implemented. A cost-optimal analysis of SOFC-based energy systems has been performed recently by Marroco et al. [13] in the frame of an EU project to determine which conditions are conducive to making SOFC-based

* Corresponding author.
E-mail address: hafsi@itae.cnr.it (Z. Hafsi).

https://doi.org/10.1016/j.ijhydene.2024.03.217
Received 13 December 2023; Received in revised form 14 March 2024; Accepted 16 March 2024
Available online 22 March 2024

energy systems a convenient option depending on the type of application (residential or non-residential) as well as for different geographical areas.Thus, due to the potential utility of SOFC technology as a component of future energy systems, optimizing their operating conditions is of crucial importance.

Basically, assessment of a SOFC technology is conducted through lab-scale testing of single cells to evaluate their electrochemical behavior, such as their characteristic I–V curves and impedance spectrum for various operating conditions (e.g. temperature and feeds) [14–16]. Consequently, these outcomes are used to design the optimal stack layout as well as to define recommended operational conditions for the integration of the SOFC stack into a power plant. Electrochemical experiments on SOFCs are likely to provide valuable insights into the optimal working potential range even without a detailed description of the gas flow at both electrodes. On the other hand, numerical modeling can play a key role in the description of some important cell parameters that affect the whole electrochemical and gas flow process within the electrodes of the cell. As a result, based on experimental data, numerical models can be a useful tool for parameterizing SOFCs i.e. estimating the characteristic parameters of the cell (e.g. exchange current densities, porosity and tortuosity of the electrodes, etc.). In literature, such approach is referred to as a calibration process [17,18]. Consequently, the optimal combination of parameters can be found to numerically reproduce the polarization curve, as well as to conduct complete cell modeling towards a deeper understanding and a more accurate description of transport dynamics within a fuel cell.

According to Yang et al. [19], SOFC performance has been predicted using a combination of experimental data and multiphysics numerical modeling. In this study, the authors attempted to calibrate cell parameters using the least amount of experimental data as possible. As a result of their work, two conclusions were drawn. First of all, relying solely on polarization curves to extract cell parameters will not yield accurate results, so polarization curves should be used in conjunction with impedance spectra to ensure that calibrated values are correct. As a support for this conclusion, the authors stated that different combinations of exchange currents could result in the same polarization; however, each combination would result in a different impedance spectrum. A second conclusion was that at least three flow conditions for oxidant and fuel utilization must be considered when modeling a cell's behavior. Those observations were also confirmed by Beale et al. [20] who claimed that varying operating temperature as well as fuel and air composition and utilization over a wide range of operational conditions is highly recommended for validation of numerical models through experimental polarization curves. An obvious way, supported also by previous related literature, is to perform the calibration process as an initial step before undertaking the modeling process in a Computational Fluid Dynamics (CFD) environment [21,22]. Nevertheless, in the literature, there are also references that rely on empirical formulas to express a variety of cell parameters and then to describe the internal mass transfer mechanisms and flow behavior within a cell electrode using CFD models [23–26]. According to the initial assumptions, desired accuracy, and symmetry of the geometry, these CFD simulations were developed under 0D, 1D, 2D, or 3D models [27–31]. However, only some of these results were confirmed through experiments with real cells after the model was developed.

The literature holds several empirical formulas for predicting SOFC parameters, but whenever experimental electrochemical testing can be conducted, the calibration approach would be preferred since it allows for better estimation of cell parameters from experimental results. Overall, whether cell parameters were obtained through calibration or from literature and empirical formulae, further CFD models are necessary to describe cell behavior in greater detail and to refine the calibrated parameters, as Yang et al. suggested [32]. Also, numerical models offer more flexibility in testing various cell geometries as well as several flow conditions. In fact, based on finite volume models, numerical studies conducted by Campanari and Iora [33,34] analyzed the effect of two SOFC geometries (i.e. tubular and planar cells) on cell performance under both isothermal and non-isothermal assumptions. In addition, CFD models were employed to describe the flow behavior and electrical performances of large scale SOFCs stack through multiphysics modeling towards optimization of working conditions once implementing large scale SOFC systems in real life applications [35–37].

Several previous studies have proposed calibration algorithms that can fit experimental electrochemical data of SOFC cells under specific working conditions. The purpose of this paper is to present a simple calibration algorithm to predict the cell parameters. Unlike most previous calibration algorithms, the presented work considers the contribution of each electrode to the cell overpotential (activation and concentration) as a separate term in the I–V curves. This approach allows one to predict morphological characteristics separately for each electrode (porosity, tortuosity, pore size diameter, etc.), instead of assuming generic mean values for those terms. Substantially, such an approach enables to extend the fitting parameters for further analysis of the flow dynamics along both electrodes via CFD tools.

Throughout this paper, a modeling approach is developed from the experimental diagnosis of a SOFC button cell fed with H_2 and air at 700 °C and 800 °C. Analytical modeling of the polarization curves [38,39] was used in the development of a calibration algorithm to determine the required parameters to evaluate various potential losses within the cell, and therefore to rebuild the experimentally measured I–V characteristic curves and to predict real cells' behavior under flexible operating conditions. By fitting the experimental polarization curve, the algorithm returned additional information about the cell's characteristics, such as exchange current densities and diffusion coefficients of the gases at both electrodes. Additionally, structural parameters of the investigated cell's electrodes were estimated through the calibration algorithm (i.e. porosities and pore size diameters). As cell parameters are highly sensitive to each other and nonlinearly coupled, they were estimated through the tuning of model variables until reaching a tradeoff that allowed numerical and experimental curves to be fitted reasonably. Although the calibrated parameters of the model fall within the range of practical values, these outcomes were defined as equivalent cell parameters. In fact, the model considers only one case of gas supply and relies on the polarization curves without accounting for the entire impedance spectrum of the cell. This is considered insufficient to characterize the obtained parameters as actual cell characteristics, as previously stated.

Hence, the paper has been organized as follows: firstly, the main mathematical formulae for evaluating various potential losses are briefly introduced, then a description of the experimental procedure is performed, and steps of the calibration algorithm are enumerated. Finally, numerically obtained polarization curves are compared to those experimentally achieved, and the equivalent cell parameters are analyzed and discussed for further refinement in potential future works.

2. Mathematical model

A simplified model of the fuel cell was considered as a steady thermodynamic system consisting of a control volume in which heat (Q) and reactants of the chemical reaction (having as enthalpy H_R) were provided as inputs, and the generated work (W) and products of the chemical reaction (having as enthalpy H_P) were collected as outputs (when used as subscripts, P and R stand for the species of products and reactants involved in the reaction respectively). Then, conservation of energy yields

$$\Delta Q - \Delta W = H_p - H_R \tag{1}$$

By denoting S_R, S_P and S_c the entropy of reactants, products, and any entropy exchanged (gained or lost) within the thermodynamic system, the entropy balance can be determined as follows:

$$\frac{\Delta Q}{T} - S_p + S_R + S_C = 0 \tag{2}$$

Combining eqs. (1) and (2), the work term ΔW can be written as follows:

$$\Delta W = \Delta Q - (H_p - H_R) \tag{3}$$

$$\Delta W = T(S_p - S_R) - TS_c - (H_p - H_R) \tag{4}$$

$$\Delta W = -\left[(H_p - H_R) - T(S_p - S_R)\right] - TS_c \tag{5}$$

Using the Gibbs free energy expression $G=H-TS$, it comes:

$$\Delta W = -\Delta G - TS_c \tag{6}$$

On the other hand, knowing that ΔW is no more than the electrical work provided by the cell, to be denoted W_e, eq. (6) is rewritten as:

$$W_e = -\Delta G - TS_c = -(G_P - G_R) - TS_c \tag{7}$$

with $G_P = \sum_{i=1}^{p} n_i g_i$ and $G_R = \sum_{j=1}^{r} n_j g_j$.

In addition, n_i and n_j are the number of moles of every species and g_i and g_j are their respective molar Gibbs free energies.

When hydrogen and oxygen are fed into a solid oxide fuel cell, the overall chemical reaction is:

$$2\,H_2 + O_2 \rightarrow 2\,H_2O \tag{8}$$

The electrical work W_e is actually the same as the energy released when two hydrogen molecules and one oxygen molecule combine to form two water molecules, which is equal to the voltage between the cell electrodes multiplied by the amount of electrical charge flowing between those electrodes per unit of time. The latter amount is proportional to the number of electrons involved in the formation of these two water molecules (four electrons are released with the formation of two water molecules). Therefore, the electrical work is written as follows:

$$W_e = 4FE \tag{9}$$

where F is the Faraday constant.

On the other hand, the change in Gibbs free energy for the reaction of eq. (8) is written in terms of initial partial pressure of involved species:

$$\Delta G = \Delta G^0 - RT \ln\left[\frac{\left(\frac{P^I_{H_2O}}{P_0}\right)^2}{\left(\frac{P^I_{O_2}}{P_0}\right)\left(\frac{P^I_{H_2}}{P_0}\right)^2}\right] \tag{10}$$

where $\Delta G^0 = -RT\,ln[K(T)]$ is the change in Gibbs free energy at equilibrium of the reaction defined by the equilibrium constant K and R is the universal gas constant. By combining eqs. (7), (9) and (10), the following relation is obtained:

$$E = \frac{RT}{4F}\ln(K) - \frac{RT}{4F}\ln\left[\frac{P_0\left(P^I_{H_2O}\right)^2}{P^I_{O_2}\left(P^I_{H_2}\right)^2}\right] - \frac{TS_c}{4F} \tag{11}$$

The term $(TS_C)/(4F)$ of eq. (11) represents the sum of potential losses (activation (η_{act}) ohmic (η_{ohm}) and diffusion (η_{diff}) overpotentials). In addition, the temperature-dependent equilibrium potential E^0can be expressed as follows [40]:

$$E^0 = \frac{RT}{4F}\ln(K) = 1.253 - 2.4516\text{x}10^{-4}T \tag{12}$$

Thus, the cell voltage equation is:

$$E = 1.253 - 2.4516\text{x}10^{-4}T - \frac{RT}{4F}\ln\left[\frac{P_0\left(P^I_{H_2O}\right)^2}{P^I_{O_2}\left(P^I_{H_2}\right)^2}\right] - (\eta_{act} + \eta_{ohm} + \eta_{diff}) \tag{13}$$

In a SOFC cell, the activation overpotential η_{act} represents the energy loss resulting from overcoming the energy barriers at each anode and cathode reaction. As a general rule, an effective cell fed with H_2 and air suffers most of its loss at the cathode due to oxygen reduction reactions, which is why the majority of research efforts focus on developing new materials for oxygen reduction reactions. Based on the Butler-Volmer equation [38,41,42], the activation overpotential in SOFC applications can be expressed using a hyperbolic sine approximation as follows:

$$\eta_{act} \cong \frac{2RT}{n_e F}\sinh^{-1}\left(\frac{i}{2i_0}\right) \tag{14}$$

where i and i_0 refer to the current density and exchange current density at equilibrium, respectively and n_e is the number of exchanged electrons per reaction.

The ohmic overpotential (η_{ohm}) results from the ionic resistance of the electrolyte and the electronic resistance of the anode and cathode and is expressed by

$$\eta_{ohm} = R_s i \tag{15}$$

Throughout the operation of a SOFC cell, R_s (in $\Omega\,cm^2$) represents the ohmic resistance associated with electronic and ionic current circulation, while i (in $A\,cm^{-2}$) represents the overall flowing current density. In an optimized SOFC cell like that investigated in this study, R_s corresponds to the electrolyte's ionic resistance, since the electrodes' electronic conductivity could be neglected. Experimentally, R_s can be deduced from the intercept of the EIS spectrum at high frequencies with the x-axis in a Nyquist plot.

Gas concentration and partial pressure decrease as gases diffuse through the porous electrode material and electrochemical reactions occur. The phenomenon of diffusion overpotential (η_{diff}) results in SOFC cells losing performance, especially at high current densities.Diffusion overpotential is due to mutual effects of Knudsen diffusion coefficient [43,44] governing the mass transfer of gas species through the pores [45–47] as well as ordinary diffusion coefficient governing mass transfer between different gas species (i.e. Fick's law). For a gas species i, of molar mass M_i, diffusing through pores (assumed to be round and straight), of mean radius r, based on kinetic gas theory [45–47], Knudsen diffusivity is given by

$$D_{i,K} = \frac{2r}{3}\sqrt{\frac{8RT}{\pi M_i}} \tag{16}$$

For the ordinary diffusion coefficient between two gases i and j, at low pressures (a condition generally met in SOFC applications), it can be evaluated using the empirical expression given by Fuller et al. [48]:

$$D_{ij} = \frac{0.00143T^{1.75}}{P\left(\sqrt{\frac{2}{\frac{1}{M_i}+\frac{1}{M_j}}}\right)\left(V_i^{1/3} + V_j^{1/3}\right)^2} \tag{17}$$

where V_i and V_j (dimensionless) stand for the diffusion volumes of gas species i and j.

The overall effective diffusion coefficient $D_{i,eff}$, of a specie i interacting with both a specie j and the medium pores, is given by Bosanquet relation [49–51] modified by a correction factor δ to take into account the medium's structure:

$$D_{i,eff} = \delta\left(\frac{1}{D_{i,K}} + \frac{1}{D_{ij}}\right)^{-1} \tag{18}$$

Generally, the factor δ is a function of the porosity and the tortuosity of the medium (often defined as the ratio of porosity ε to tortuosity τ [45–47]). A simpler form of the correction factor $\delta = \varepsilon^{1.5}$ was given by Bruggerman [42].

In the simplified case of a SOFC cell with optimized porosity in both electrodes that operates at pressures near ambient, the diffusion over-

potential for the anode and cathode can be written, as a function of effective diffusion coefficient in the anode $D_{a,eff} = \frac{P_{H_2O}}{P_a} D_{H_2,eff} + \frac{P_{H_2}}{P_a} D_{H_2O,eff}$ and in the cathode $D_{c,eff} = D_{O_2,eff}$, under the form [38,52,53]:

$$\eta_{diff,a} = \frac{RT}{2F} \ln \left(\frac{1 + \frac{RTl_a}{2FD_{a,eff} P^I_{H_2O}} i}{1 - \frac{RTl_a}{2FD_{a,eff} P^I_{H_2}} i} \right) \tag{19}$$

$$\eta_{diff,c} = -\frac{RT}{4F} \ln \left[\frac{\frac{1}{\chi_{O_2}} - \left(\frac{1}{\chi_{O_2}} - P^I_{O_2} \right) \exp \left(\frac{RT\chi_{O_2} l_c}{4FD_{c,eff}} i \right)}{P^I_{O_2}} \right] \tag{20}$$

where l_a and l_c refer to the thicknesses of the anode and the cathode respectively and the coefficient δ_{O_2} is written as a function of the Knudsen diffusivity of O_2 [54]

$$\chi_{O_2} = \frac{D_{O_2-K,eff}}{D_{O_2-K,eff} + D_{O_2,eff}} \tag{21}$$

By combining eq. (13) and eqs. 14–21, the expression for cell voltage as a function of current density and reaction parameters is obtained as follows:

$$\begin{aligned} E = 1.253 - 2.4516\text{x}10^{-4} T - \frac{RT}{4F} \ln \left[\frac{P_0 \left(P^I_{H_2O} \right)^2}{P^I_{O_2} \left(P^I_{H_2} \right)^2} \right] \\ - \left[\begin{array}{l} \frac{2RT}{n_e F} \sinh^{-1} \left(\frac{i}{2i_{0,a}} \right) + \frac{2RT}{n_e F} \sinh^{-1} \left(\frac{i}{2i_{0,c}} \right) + \\ R_s i + \frac{RT}{2F} \ln \left(\frac{1 + \frac{RTl_a}{2FD_{a,eff} P^I_{H_2O}} i}{1 - \frac{RTl_a}{2FD_{a,eff} P^I_{H_2}} i} \right) - \\ \frac{RT}{4F} \ln \left[\frac{\frac{1}{\chi_{O_2}} - \left(\frac{1}{\chi_{O_2}} - P^I_{O_2} \right) \exp \left(\frac{RT\chi_{O_2} l_c}{4FD_{c,eff}} i \right)}{P^I_{O_2}} \right] \end{array} \right] \end{aligned} \tag{22}$$

3. Experimental setup and numerical procedure

An important outcome of laboratory scale tests for SOFCs is the polarization curve and electrochemical impedance spectrum. Although providing information about the highest cell performance point and the range of currents and voltages the cell can cover, these diagnoses do not provide a full understanding of charge and mass transfer, and the internal flow of reactants on the anode and cathode sides.

To analytically plot the current-potential characteristic curve for the SOFC, knowledge, or at least an estimation with an acceptable tolerance, of all parameters occurring in eq. (22) is required. From this equation, four types of parameters can be distinguished: i) parameters known without conducting any experiment (geometric parameters and initial conditions), such as l_a, l_c, $P_{H_2O}{}^I$, $P_{H_2}{}^I$, $P_{O_2}{}^I$, T, and P_0; (ii) parameters that can be calculated numerically using empirical formulae as for $D_{a,eff}$ and $D_{c,eff}$; (iii) parameters that can be calculated using Electrochemical Impedance Spectroscopy (EIS) as R_s; iv) parameters requiring numerical testing as $i_{0,a}$ and $i_{0,c}$. The latter parameters are considered as targets in the development of the calibration algorithm. Furthermore, it is important to note that since the assessment of effective diffusion coefficients involves the prediction of a correction factor that is dependent on the porous medium structure, this parameter has also been taken into account numerically through the fitting of the polarization curve.

In the following subsection, a brief description of the experimental setup and characteristics of the tested cell, as well as the main calibration steps are introduced.

3.1. Materials and experimental setup

Experimental measurements were carried out on a 7 mm radius anode supported button cell, which was laser cut from a large area planar cell. The electrolyte, the anode and the cathode are made up respectively of Yttria-Stabilized Zirconia (YSZ), Nickel Oxide-Yttria-Stabilized Zirconia NiO/YSZ and Lanthanum Strontium Cobalt Ferrite mixed with Gadolinium-Doped Ceria (LSCF/GDC). Various cell parameters and experimental conditions are reported in Table 1.

This button cell was mounted between two alumina tubes on a Greenlight Innovation test bench with a pneumatic system for loading pressure against two Thermiculite o-rings between which the cell was positioned. The pneumatic system also ensures a proper electrical connection because the alumina tubes have inside other mobile alumina tubes for feeding gas and supporting gold grids attached to gold wires. In order to make measurements using the 4-point method, two gold wires are connected to each electrode. The main alumina tubes also contain two thermocouples (one for the anode and one for the cathode sides), which were used to set the cell temperature precisely. A Metrohm Autolab is externally connected to these 4-gold wires for conducting electrochemical experiments on the SOFC cell. A procedure aimed at achieving a complete reduction of NiO was performed as a first step. During such a step, the cell was fedwith 10% H_2 in He for 3 h at 800 °C. Consequently, a stable open circuit voltage (OCV) value and reproducible spectra on the EIS measurements demonstrate complete cell reduction. Afterwards, experiments were conducted at 700–800 °C feeding humidified hydrogen (3 vol% water) at the anode at a flow rate of 50 sccm, and dry air at a flow rate of 125 sccm at the cathode. The electrochemical measurements included polarization curves, electrochemical impedance spectroscopy at different potentials, and durability tests.

3.2. Calibration algorithm

To develop a calibration algorithm, two main results of the experiments were considered, namely the polarization curve, which is used as a benchmark to fit a numerically derived curve with, and the series resistance determined from the EIS spectrum (the intercept between the EIS spectrum at high frequency and the x-axis). As a result of solving eq. (22), the final optimized curve is influenced by the synergistic effects of activation and diffusion losses governed by the interplay between exchange current densities and effective diffusion coefficients that are the algorithm's main target parameters. In addition, the series resistance from experiments is used for evaluating ohmic losses prior to calibration.

Regarding diffusion losses, it is noteworthy that the parameter r appearing in the expression of Knudsen diffusivity is itself an unknown structural parameter that must be estimated. Additionally, the

Table 1
Parameters of the model and experimental conditions.

Parameter		Value
Cell Radius (mm)		7
Working temperature (°C)		700; 800
Electrolyte thickness (μm)		13
Anode side		
	Thickness (μm)	400
	Volume fraction of H_2	0.97
	Volume fraction of H_2O	0.03
	Diffusion volume of H_2 (−)	6.12
	Diffusion volume of H_2O (−)	18.5
Cathode side		
	Thickness (μm)	24
	Volume fraction of O_2	0.21
	Volume fraction of N_2	0.79
	Diffusion volume of O_2 (−)	16.3
	Diffusion volume of N_2 (−)	13.1

correction factor δ of eq. (18) introduced to evaluate the effective diffusion coefficient is a structural correction parameter that is influenced by electrode morphology (porosity and tortuosity) and is used primarily to adjust the Knudsen diffusivity. As a result, the pore radius parameter r can be included in the diffusivity correction factor (denoted ξ), so that effective Knudsen diffusivity can be written as:

$$D_{i,K,eff} = \xi \sqrt{\frac{8RT}{\pi M_i}} \tag{23}$$

with $\xi = \delta(2r/3) = \varepsilon^{1.5}(2r/3)$

When the correction factor ξ is known, along with the specific surface area SSA and density ρ of powder materials of the anode and cathode, the porosity and mean pore radius for both electrodes can be determined by combining the expression of ξ with the following equation:

$$r = \frac{2\varepsilon}{\rho SSA} \tag{24}$$

Nevertheless, and due to lack of information about the characteristics of the powder materials (SSA and ρ) forming the anode and the cathode of the tested cell, the developed algorithm considers the pore radii of the anode and the cathode as extra target parameters that were searched for. Hence, the values of porosities of the anode and cathode are estimated and discussed.

Therefore, the calculation algorithm was implemented in Matlab along with the input functions through the following steps.

i. Definition of parameters.
ii. Evaluation of ordinary diffusion coefficients of species in the anode and cathode sides: implementation of a Matlab function to evaluate ordinary diffusion coefficients of various gases as defined by eq. (17).
iii. Evaluation of Knudsen diffusion coefficients of species at both electrodes.
iv. Calculation of diffusion coefficient in the anode and in the cathode sides.
v. Evaluation of the theoretical value of the OCV.
vi. Import of experimental EIS data and evaluation of the series resistance.
vii. Import of experimental data of the polarization curve.
viii. Define ranges (upper boundaries and lower boundaries) for the target parameters to be searched for: anode and cathode exchange current densities ($i_{0,a}$ and $i_{0,a}$), correction factor for the diffusion coefficient in the anode and the cathode sides (δ_a and δ_C), pore size radii in the anode and cathode sides (r_a and r_c).
ix. Define as an objective function the absolute value of the difference between the theoretical cell potential (eq. (22)) and the experimental one.
x. Run the algorithm of interior point method [55] through the prebuilt MATLAB function *fmincon* in order to minimize the defined objective function.
xi. Retain obtained values of the target parameters that minimize the objective function and evaluate the overall mean error between numerical and experimental cell potential. The obtained target parameters are compared to common practical values and then retained as equivalent cell parameters.

According to step viii, the range of each target parameter defines the interior (feasible) region within which the interior point method will be applied, i.e. the parameters leading to the calibration algorithm's solution.

4. Results and discussion

4.1. Validation of the fitting model

As a first step, the algorithm is applied to the cell operating at 800 °C. Fig. 1 shows the plot of the experimental impedance spectrum at the OCV (1.056V was the measured voltage) to determine the series resistance. As a result of these conditions, the series resistance was determined to be 0.144 Ω cm^2. In general, such a value corresponds to the electrolyte resistance since O^{2-} transport is more energy-demanding than electrons that pass-through electrodes during cell operation. Because of this, most manufacturers strive to produce cells with as thin an electrolyte as possible. Because R_s depends mostly on the conductivity of the electrolyte, it should remain constant even with varying potentials if the temperature remains constant. Ideally, this is true except when there is a partial loss of electronic conductivity within the electrodes, for instance because of unoptimized or aged cells.

As shown in Fig. 2, the experimental I–V curve was collected up to 0.3 V to prevent extensive reoxidation of the anode due to the irreversible nature of Ni. This figure also includes power density curve plotted against the current density. A maximum power density of about 0.7 W cm^{-2} was achieved by the cell at about 0.5 V, and its I–V curve was characterized by at least three slopes associated with activation, ohmic, and diffusion constraints, which concurred to the irreversibility of this electrochemical process. Therefore, the subsequent calibration algorithm was kept running until it reached the most accurate fit within acceptable tolerances, as outlined in Fig. 2, in order to evaluate other cell potential losses beyond R_s.

Similarly, tests were performed at 700 °C. A comparison of the EIS spectra recorded at OCV (in this case, 1.078 V) and 800 mV is shown in Fig. 3. It is noticeable that the features of EIS change with voltage value. Specifically, at 0.8 V the entire spectrum contracts and this is a direct consequence of cell polarization. At OCV, electrochemical reactions at both electrodes are strongly affected by the activation constraint, and the profile shows a dominant semicircle associated with the more energy-consuming mechanism. If compared to EIS spectrum measured at 800 °C (Fig. 1), this behavior is particularly striking.Generally, when an optimized SOFC cell operates with H_2 and air, the reduction of O_2 is the most energy-consuming reaction, explaining why one semicircle dominates the EIS spectrum. In the spectra at 0.8 V, there were two well defined semicircles associated with the anode and cathode reactions. Depending on the materials used for SOFCs manufacturing, theseare a characteristic feature of H_2 oxidation and O_2 reduction. Therefore, the fact that only one semicircle dominates the EIS at OCV can be attributed to the limited activity of LSCF perovskite used as cathode when the cell is placed at OCV. At 700 °C, however, the R_s remained unchanged

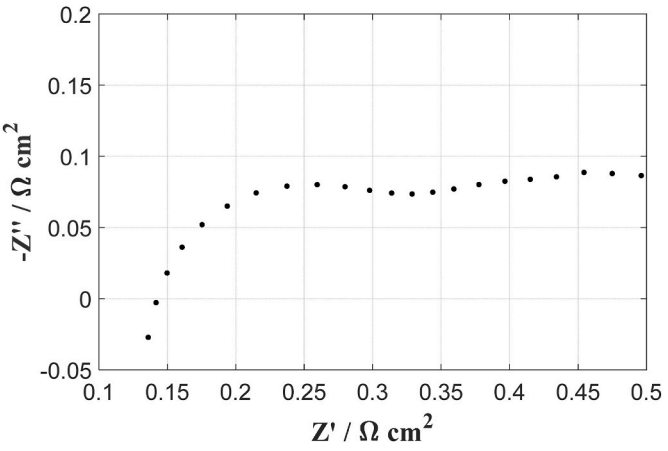

Fig. 1. A magnification of the impedance spectrum profile of the investigated SOFC cell at OCV and during its operation at 800 °C.

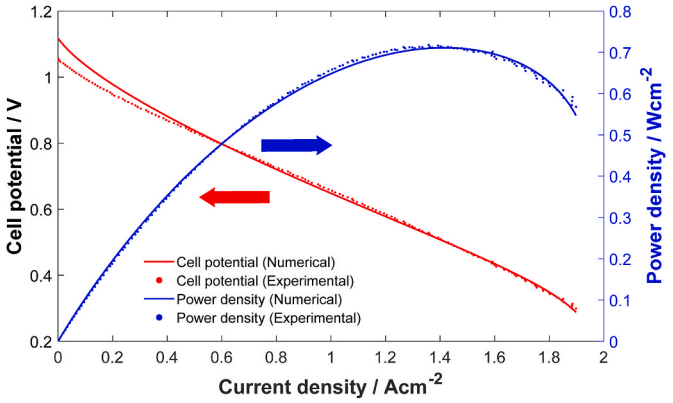

Fig. 2. Comparison of experimental and numerically fitted polarization curves at 800 °C.

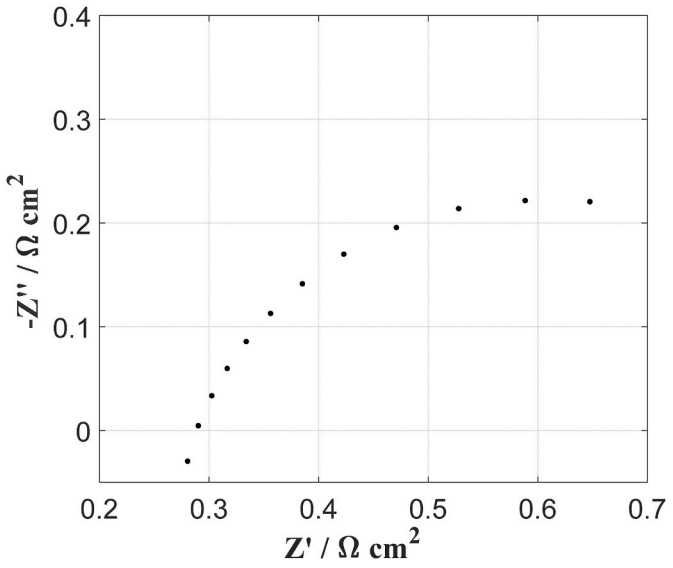

Fig. 3. A magnification of the impedance spectrum profile of the investigated SOFC cell at OCV during its operation at 700 °C.

regardless of the potentials used for measurement, with a value of 0.294 Ω cm^2.

In general, an EIS spectrum can be fitted by an electrical circuit simulating the mechanisms occurring in a cell during operation and providing information about the number of reactions, any possible bottlenecks, associated mechanism kinetics as well as suggestions for improving them [2,56]. The simulating of EIS is beyond the scope of this paper. However, from comparing EIS spectra, it became apparent that the main constraining reaction for an optimized cell such as the one investigated in this study was the reduction of oxygen.

To fit the experimentally measured I–V curve at 700 °C, the same diffusivity correction factors used for the 800 °C I–V curve model were applied. This is due to the Bruggerman relation that assumes δ independent of temperature. Obviously same pore radii obtained for T = 800 °C are retained and the model was run only to determine exchange current density values. As shown in Fig. 4, the calibrated polarization curve is plotted alongside with that obtained experimentally.

In accordance with this characteristic curve, the maximum performance was reached at 470 mV with a power density of 372 mW cm^{-2}, which was slightly higher than half of the maximum performance measured for the cell operating at 800 °C that was achieved at 520 mV. Accordingly, by comparing the cell behavior at two different temperatures investigated, there was a significant reduction in performance at

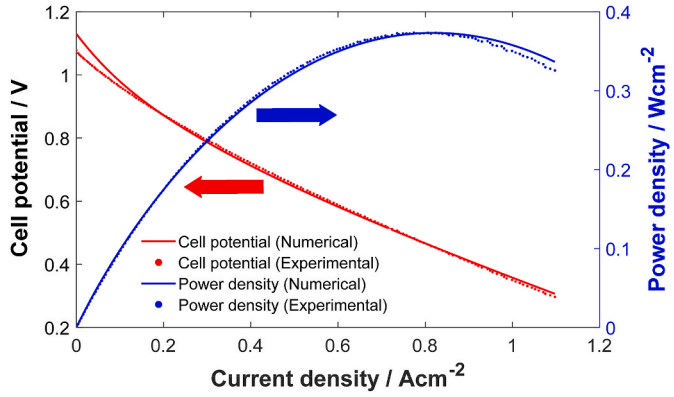

Fig. 4. Comparison of experimental and numerically fitted polarization curves at 700 °C.

700 °C along with a significant reduction in efficiency, which occurred at first as a result of the high potential drop observed up to 200 mA cm^{-2}. Cell performance is generally affected by the activation control at low current density, which, at 800 °C, resulted in a loss of potential of approximately 100 mV, and at 700 °C, in a loss of approximately 200 mV. Furthermore, the increased resistance of the electrolyte may also be responsible for the performance loss at 700 °C. As determined by the EIS, the R_s was 0.145 Ω cm^2 @ 800 °C and 0.294 Ω cm^2 @ 700 °C.

In terms of the calibration algorithm, Figs. 2 and 4 demonstrate that the numerical analyses have been able to determine the equivalent target parameters of interest (exchange current densities and diffusion coefficients) with a high degree of accuracy, with errors ranging between 1.2 % and 1.4 %. This error is mainly caused by a discrepancy between the experimental and fitted curves in the region of low current density. The main reason for such divergences was the difference between experimental and analytically evaluated OCV values. Based on the Nernst equation (eq. (13)), the expected values were slightly higher than those determined experimentally (1.1174 V vs. 1.056V at 800 °C and 1.13V vs. 1.078V at 700 °C). Most previous literature [57] attributes this difference to one or more effects occurring under experimental conditions and in compliance with: i) current leakage (this phenomenon is typically observed for gadolinia doped ceria as a result of the redox transition $Ce^{4+} \rightarrow Ce^{3+}$); ii) gas leakage caused by unoptimal sealing, such as when using a compressive gasket, causing changes in partial pressures and in the Nernst equation; iii)) crossover of gases through the possible defects in the electrolyte that results in the partial mixing of anodic and cathode gases, leading to a mixed potential for the cell.

For such a situation, the activation losses formula is usually slightly modified by adding an extra current density term i_{ex} to the expression of eq. (14) that becomes:

$$\eta_{act} = \frac{2RT}{n_e F} \sinh^{-1}\left(\frac{i + i_{ex}}{2i_0}\right) \tag{25}$$

However, this effect was not taken into account in this model because multiple phenomena can occur during experiments, which would further overload the calculation algorithm. Furthermore, these differences are only evident in the low current density range, mainly affecting the activation control region of the I–V curves. According to the plots of power density curves, even without accounting for internal leakage, the experimental and modeled curves match sufficiently well even at low current densities. The reason for such evidence can be attributed primarily to the low current density in the region where the drop in OCV was observed. Secondly, since the activation loss depends on the slope of the curve at near zero current density according to the Butler-Volmer equation (eq. (14)), a lower inclination of the I–V curve produces a lower activation loss. Then, although the current leakage dropped the experimental OCV value compared to the theoretical one, the ratio $V_{numerical}/V_{experimemtal}$ is always inversely proportional to the

ratio $I_{numerical}/I_{experimemtal}$ and the loss of voltage is compensated by an increase of current causing the power density to not being significantly affected by the current leakage at low current densities (below 200 mA cm^{-2}). Consequently, as shown in Fig. 4, power density curves are well fitted mainly near zero current density.

In Table 2, the mean error evaluated between the fitted and the experimental polarization curves is reported. This table also shows the numerically calculated maximum power density that is substantially in agreement with the experimentally measured values, this agreement can be considered as a further evidence of this fitting procedure's effectiveness.

4.2. Exploitation of the calibrated model

The I–V curves were collected in the potential range from OCV to 0.3 V. For practical reasons, it was preferred not to extend the tests up to short circuit to avoid damaging the cells. It will be discussed in more detail later that the extremely low cell potential corresponds to extensive reoxidation of Ni and that this can lead to cracks in the cell. As well, it is not recommended to operate under a diffusional regime as it typically occurs at lower voltages than 0.4 V, resulting in a decay in performance and low efficiency. In spite of this, the characteristic curve measurement was extended to 0.3 V only for the time required for recording the data necessary for the calibration algorithm. However, once the modelling algorithm has properly fitted the experimental data, as in this study, it is possible to extend the simulation results up to the short circuit voltage so that the maximum current density can be determined. Furthermore, extending the polarization curve plot to short circuit is a useful way to highlight the effect of diffusion losses at high current density, as shown in Fig. 5. In this figure, an I–V curve derived from an experiment carried out at 800 °C was split over multiple overpotentials and plotted versus the current density. In terms of activation overpotentials, the cathode showed a higher drop in the entire current range as expected. Despite the high temperatures, the cathode reaction in a commercial cell operating with H_2 and air is usually more energy intensive and the slowest step in the overall electrochemical conversion process. The reason for this is primarily because oxygen molecules have a higher binding energy than hydrogen molecules. Moreover, due to the different number of electrons involved in the formation of stable ionic species, O_2 reduction has a lower probability than H_2 oxidation (which is also boosted by the presence of high reactive species):

$$anode : H_2 + O^{2-} \rightarrow H_2O + 2\,e^- \tag{26}$$

$$cathode : \frac{1}{2}O_2 + 2\,e^- \rightarrow O^{2-} \tag{27}$$

However, the anode and cathode losses increase as current density increases, and this can be attributed to the redox reactions occurring at the electrodes during operation. The trend of the ohmic loss can also be attributed to these modifications. As a result of irreversible energy conversion, a reduction in cell voltage leads to an increase in cell temperature. According to the ohmic law, an increase in local temperature could enhance ionic conductivity in the electrolyte while reducing electronic conductivity in the electrodes. However, for an optimized cell like that studied here, the electrolyte resistance is higher than that of the electrodes. Thus, increasing ohmic resistance with current density

Table 2
Evaluation of the accuracy of the calibrated model.

Parameter of evaluation		@ 700 °C	@ 800 °C
Mean error of calibration		1.229%	1.348%
Performance point (peak power density)	Experimental	(0.373 W cm^{-2} @ 0.470 V)	(0.714 W cm^{-2} @0.519V)
	Numerical	(0.373W cm^{-2} @ 0.455V)	(0.711W cm^{-2} @ 0.503V)

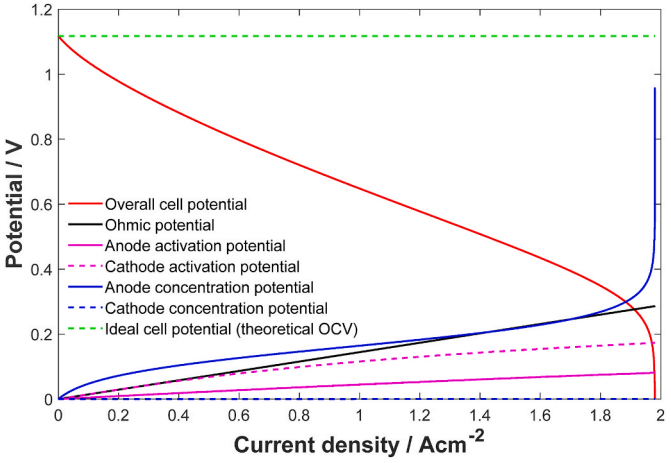

Fig. 5. Calculated polarization curve and associated overpotentials for the experiment at 800 °C.

should have a different purpose. In the anode, increased current density should result in Ni being oxidized by water:

$$Ni + H_2O \rightarrow NiO + H_2 \tag{28}$$

As a result, this electrode becomes less conductive and the kinetic for H_2 oxidation becomes more difficult. However, on the cathode side, reducing conditions result in oxygen ions being lost and a redox mechanism produces a structural transition from perovskite to Ruddlesden-Popper phase, resulting in a partial loss of electronic conductivity and kinetic promptness towards oxygen reduction. Substantially, the circulation of current causes structural changes on the electrodes, which lead to increased ohmic and activation losses.

Regarding the diffusional constraint, it was observed that the effect is virtually negligible at the cathode, while it is prominent at the anode. Clearly, this behaviour was due to the design of a SOFC's cell and its operating mechanism. In a commercial cell like the one studied in this work, the cathode is extremely thin and contains a high concentration of triple phase boundaries (TPBs). Further, since the cathode is made of ferrite-based perovskite, a well-known mixed ionic and electronic conductor (MIEC), there is a high region within which O_2 reduction can take place within this electrode.

The anode, on the other hand, is the support of the investigated cell. Its thickness is designed to resist mechanical solicitation occurring during cell operation. In this electrode, besides oxidizing H_2, products of the reaction are generated (according to eq. (26)). Furthermore, considering the nature of this material known as cermet, TPB concentrations should be highest at the interface between anode and electrolyte, the region where hydrogen oxidation is most likely to occur. Thus, the diffusion constraint at the anode results from the combination of these electrode characteristics and is minimally affected by the Knudsen mechanism through the anode porosity, while the Fick's law significantly affects H_2 diffusion due to the obstructive action caused by the water formed during the electrochemical reaction.

The numerical modelling of the I–V curve measured at 700 °C (Fig. 6) produced curves with similar trends to those measured at 800 °C, despite slight differences noted. In terms of activation overpotentials, anode behavior showed significant constraint due to a lower kinetic for the redox reaction involving the transition $Ni \leftrightarrow Ni^{2+} + 2\,e^-$. Clearly, this constraint increases as water is generated by the electrochemical reaction. In spite of this, reduced temperatures have accelerated the degradation of cathode activation. As it is well known, ferrite-based perovskites exhibit quite satisfactory electrochemical behavior at high temperatures, whereas their ability to reduce oxygen at low temperatures is still challenging. As a result, at high current density the cathode loss affects the I–V curve for about 300 mV. Nevertheless, the major loss

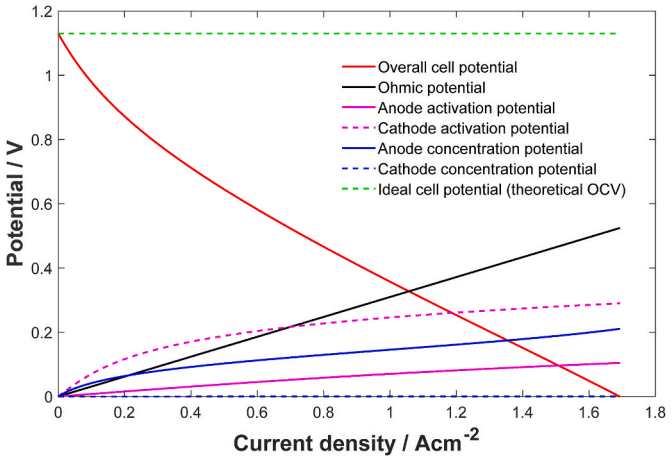

Fig. 6. Calculated polarization curve and associated overpotentials for the experiment at 700 °C.

is accounted for by the ohmic overpotential that controls the I–V curve at high current density for about 500 mV. As discussed for the trend observed at 800 °C, the increase in ohmic loss can be attributed mainly to redox mechanisms occurring in the electrodes that cause conductivity degradation. Clearly, at 700 °C, transitions leading to restoration of the initial phases in electrodes occur at a slower rate, resulting in a faster decline than at 800 °C. Nonetheless, the profile of the curve at 700 °C near the short circuit was significantly different from that at 800 °C in the region of high current densities. In this curve, the dramatic loss of performance observed for the anode at 800 °C at current densities greater than 1.9 A cm^{-2} was not identified. As for the cathode, the profile of concentration loss was substantially the same as that at 800 °C. It is likely that the anode behaves differently at these two temperatures due to the difference in maximum current density achieved at short circuit. It is a consequence of the high ohmic loss at 700 °C.

Fig. 7 compares overpotential curves at 700 and 800 °C to illustrate differences and possible temperature dependent effects. Comparing these curves, it is apparent that the activation control at 700 °C was intensely sloped in the first 400 mA cm^{-2}. Following that, the trend was similar to the experiment conducted at 800 °C. This intense loss at low current density is explained by ferrite-based perovskites having limited electrocatalytic activity especially at intermediate temperatures, as it is extensively reported in the literature. Developing novel cathodes [58–60] is expected to further improve this behavior. Despite this, ohmic loss appeared to have the strongest impact on cell performance in

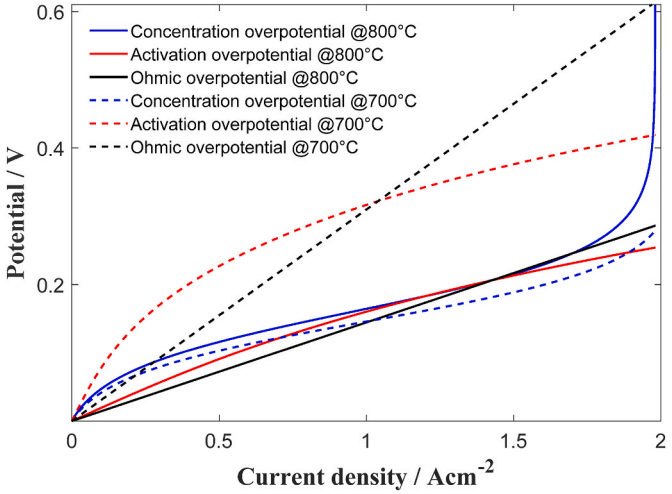

Fig. 7. An overview of different potential losses at 700 °C and 800 °C.

the investigated current density range. At 700 °C, the intense slope of the ohmic loss is caused by the limited kinetics of the redox mechanisms required for restoring the conductive phases of the anode and cathode. As a result, current challenges concern developing novel electrolytes [61,62] and developing cells with thin electrolyte layers [63,64], while redox-enhanced electrodes have made limited progress and it is a current challenge [65–67]. In terms of concentration loss, the curves at the two temperatures were similar. It is evident from their similar trends that temperature had a limited influence on them. However, a notable deviation was observed in their similar trends near the cell short circuit, where the high current density circulating at 800 °C triggered a dramatic increase in this loss. An intense current density close to 2 A cm^{-2} circulated in the cell near the short circuit at 800 °C, according to the experimental curve. As a result, the partial pressure of H_2O increased dramatically, which led to a blocking effect for H_2, preventing its approximation to the electrode-electrolyte interface. This effect, however, can be improved substantially by optimizing the electrodes' morphology in accordance with porosity, tortuosity, and pore diameters. Literature suggests that an optimal SOFC cell should have pores ranging between 0.012 μm and 0.5 μm, porosities between 0.1 and 0.7, and tortuosity between 2 and 20 [53,68–72]. Due to this, manufacturers are particularly concerned with designing cells with appropriate morphologies, as well as satisfying mechanical and electrical requirements. In fact, optimizing the concentration potential to the lowest possible values is likely to broaden the range of current density the cell can cover (increase of the limiting current density) and thus increase the cell's lifetime and suitability for various applications (such as generating electricity during fuel cell mode or hydrogen during electrolysis mode).

Further discussion of the concentration potential's evolution with temperature is presented in the following section.

4.3. Estimated equivalent cell parameters: evaluation and discussion

Having validated the numerical curve through fitting of data, equivalent cell parameters were evaluated to replicate the experimental data. The present model examines the diffusion coefficients and exchange current densities at both electrodes. A number of empirical formulae are reported in the literature to calculate exchange current densities by fitting experimental data to an Arrhenius type correlation. The following is a commonly used form [73]:

$$i_{0,e} = \frac{RT}{n_e F} k_e \exp\left(\frac{-E_{a,e}}{RT}\right) \tag{29}$$

where k_e ('e' stands for electrode: anode or cathode) is a pre-exponential factor and $E_{a,e}$ is the activation energy (a value of $E_{a,a} = 140$ kJ/mol for the anode and $E_{a,c} = 137$ kJ/mol for the cathode as reported in the literature was considered for this study [73]).

Considering eq. (29), the values of target parameters of interest as

Table 3
Main outputs of the calibrated model: equivalent cell parameters.

Output parameters	T = 700 °C	T = 800 °C
Equivalent anode exchange current density $i_{0,a}$ (Acm^{-2})	0.530	0.998
Pre-exponential factor k_a for $i_{0,a}$ expression ($\Omega^{-1}cm^{-1}$)	4.138e+10	1.409e+10
Equivalent cathode exchange current density $i_{0,c}$ (Acm^{-2})	0.053	0.312
Pre-exponential factor $k_c$for $i_{0,c}$ expression ($\Omega^{-1}cm^{-1}$)	5.739e+9	6.288e+9
Equivalent anode diffusivity correction parameter δ_a	0.0886	
Equivalent cathode diffusivity correction parameter δ_C	0.1987	
Equivalent anode pore size radius (μm)	0.0568	
Equivalent cathode pore size radius (μm)	2.6797	
Equivalent anode porosity	0.2[a]	
Equivalent cathode porosity	0.34[a]	
Limiting current density (Acm^{-2})	1.693	1.981

[a] Porosity values evaluated using Brugermann relation $\delta = \varepsilon^{1.5}$.

well as limiting current densities, and pre-exponential factors for exchange current densities are summarized in Table 3.

Equivalent parameters obtained from the experimental data are further examined in terms of their order of magnitude and the extent to which they reflect the physical behavior of current cell parameters. According to Table 3, equivalent parameters referring to exchange current densities have the same order of magnitude as values of current densities reported in literature [70]. Additionally, cathode exchange current density for H_2/air fed SOFCs is generally lower than anode exchange current density [74,75] and both increase with temperature, enhancing the kinetics of H_2/O_2 redox mechanisms.

As for the pore size radius, despite being of different orders of magnitude for the porous anode and cathode electrodes, equivalent values obtained were comparable to those reported in literature [68]. A further focus on the structural parameters of porous electrodes is implemented by evaluating the porosities of the cathode and the anode under the Brugermann assumption where the effect of tortuosity is not included [42] as reported in Table 3. Moreover, it is reported in the literature [38,47,76] that diffusivity correction factor can be evaluated as the ratio of porosity to tortuosity. Accordingly, when tortuosity τ is 2 for cathode [29] and 5.4 for anode [53], then cathode porosity is about 0.4 and anode porosity is about 0.48. Therefore, the porosity values reported in Table 2 are within the range of common values encountered in literature.

Temperature and current density are examined in relation to concentration potential using equivalent pore radii on the anode and cathode sides to evaluate diffusion coefficients for various species. According to Fig. 8, the concentration potential is plotted as a function of temperature and current density. As shown in the 2D plot of this figure, the concentration overpotential is barely influenced by temperature at low current densities, and becomes more affected by temperature at high current densities. The behavior shown in Fig. 8 is directly related to the mechanism involved in the diffusion of species towards the reactive regions represented by the TPBs at the electrode-electrolyte interface. Particularly the anode is subjected to similar conditions, being the electrode where electrochemical reaction products are generated. Furthermore, since its thickness provides support to the cell, therefore producing constrain to the diffusion of species. Electrochemical reaction products are responsible for a significant part of the performance degradation caused by the Fick law limitation, where temperature has a limited influence. Further, the anode constrains species diffusivity due to its thickness, which is required for robust cell manufacturing. This is the reason why manufacturers [63,77–81] generally produce cells with a graded composition in the anode and more precisely with a functional layer near the electrolyte where the cermet (Ni-YSZ) composition is slightly overloaded with ceramic (YSZ) to increase the concentration of TPBs and to enhance the open structure to promote Knudsen diffusivity within the pores.

5. Conclusions

On the basis of experimental data obtained with a commercial SOFC operated in the presence of H_2 and air at 700 °C and 800 °C, this study developed an analytical method for estimating equivalent SOFC operational parameters. By applying the fitting algorithm, polarization curves are used to generate calibrated parameters that allowed numerically replicating as well as analysing the I–V curves. Using the available literature data, the achieved parameters were discussed and largely agreed upon. Moreover, since the model considers the effects of each electrode separately on potential losses, obtained parameters describing electrode structures and exchange current densities can be further exploited and incorporated into detailed CFD models. As an exploitation of these results, in this paper, a discussion of the mechanisms occurring within the cell and the cell's performance, including constraints and possible actions for achieving advantages in terms of manufacturing procedures and operating conditions, was presented. Even though,

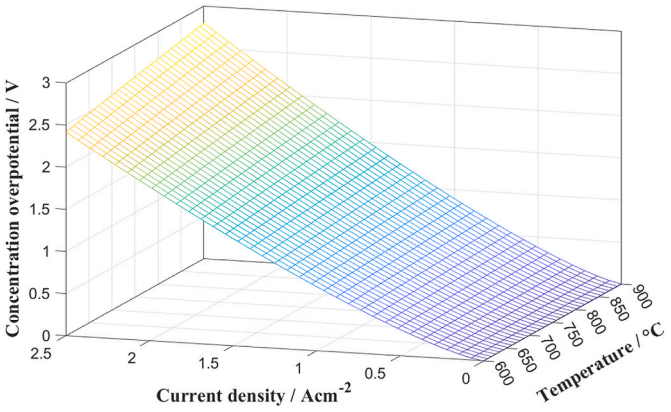

Fig. 8. Concentration overpotential as a function of temperature and current density.

further analysis may be required to ensure that these parameters accurately reflect experimental cells' characteristics across a wide range of applications. Currently, further experimental testing is being conducted to validate the algorithm under different fuel and oxidant supply conditions, as well as analyzing the cell impedance spectrum. CFD models based on such results could provide deeper insight into electrochemical behavior of cells and gas flow mechanisms into stack manifolds. Consequently, this paper represents the first step towards developing reliable CFD models for predicting optimal SOFC operation conditions, that would be of major interest when it comes to develop novel and more reliable energy technologies. Using this methodology, different scenarios of energy consumption can be evaluated in advance to ensure safety and efficiency once the SOFC stacks are integrated into the power grid.

CRediT authorship contribution statement

Zahreddine Hafsi: Conceptualization, Data curation, Formal analysis, Methodology, Software, Validation, Writing – original draft. **Sebastian Vecino-Mantilla:** Conceptualization, Data curation, Methodology, Validation. **Massimiliano Lo Faro:** Formal analysis, Funding acquisition, Methodology, Project administration, Resources, Supervision, Validation, Writing – review & editing.

Declaration of competing interest

The authors declare that they have no known competing financial interests or personal relationships that could have appeared to influence the work reported in this paper.

Acknowledgements

This research was funded by the European Union – NextGeneration EU from the Italian Ministry of Environment and Energy Security POR H2 AdP MMES/ENEA with involvement of CNR and RSE, PNRR - Mission 2, Component 2, Investment 3.5 "Ricerca e sviluppo sull'idrogeno", CUP: B93C22000630006.

In addition, the authors acknowledge the MUR for funding the PRIN project SUPERH2, CUPE53D23009400006 and PRIN PNRR project OxCellenT, CUP B53D23027440001.

Dr. Hafsi acknowledges the ITELECTROLAB, the Joint lab between CNR-ITAE and IQSC-USP financed by the National Research Council of Italy (CNR) and the Dr. Lo Faro acknowledges the bilateral project "FlexPower- Solid Oxide Fuel Cell fed with Biofuel as an Electric FlexibleProvider in a Distributed Grid" granted by MAECI.

References

[1] Singhal SC. Solid oxide fuel cells, history. In: Kreysa G, Ota K-i, Savinell RF, editors. Encyclopedia of applied electrochemistry. New York, New York, NY: Springer; 2014. p. 2008–18.
[2] Lo Faro M, Campagna Zignani S, Vecino-Mantilla S, Arico' AS. A simple approach to make the commercial solid, oxide fuel cells flexible in the use of fuels – CK-3L05. Ceram Int 2023;49:24469–74.
[3] La Rosa D, Lo Faro M, Monforte G, Antonucci V, Arico AS. Comparison of the electrochemical properties of intermediate temperature solid oxide fuel cells based on protonic and anionic electrolytes. J Appl Electrochem 2009;39:477–83.
[4] Lo Faro M, Arico AS. Electrochemical behaviour of an all-perovskite-based intermediate temperature solid oxide fuel cell. Int J Hydrogen Energy 2013;38:14773–8.
[5] Lo Faro M, Cantane DA, Naro F. In the path for creating Research-to-business new opportunities on green hydrogen between Italy and Brazil. Int J Hydrogen Energy 2023;48:11876–84.
[6] Dixon J, Bell K, Brush S. Which way to net zero? a comparative analysis of seven UK 2050 decarbonisation pathways. Renew Sustain Energy Transit 2022;2:100016.
[7] Zhao X, Ma X, Chen B, Shang Y, Song M. Challenges toward carbon neutrality in China: strategies and countermeasures. Resour Conserv Recycl 2022;176:105959.
[8] Sun L-L, Cui H-J, Ge Q-S. Will China achieve its 2060 carbon neutral commitment from the provincial perspective? Adv Clim Change Res 2022;13:169–78.
[9] Le A, Rodrigo N, Domingo N, Senaratne S. Policy mapping for net-zero-carbon buildings: insights from leading countries. Buildings 2023;13:2766.
[10] Hansen JB, Christiansen N. Solid Oxide Fuel Cellssolid oxide fuel cell (SOFC), Marketing Issuessolid oxide fuel cell (SOFC)marketing issues. In: Meyers RA, editor. Encyclopedia of sustainability science and technology. New York, New York, NY: Springer; 2012. p. 9904–33.
[11] Chan CY, Rosner F, Samuelsen S. Techno-economic analysis of solid oxide fuel cell-gas turbine hybrid systems for stationary power applications using renewable hydrogen. Energies 2023;16:4955.
[12] Ippommatsu M, Sasaki H, Otoshi S. Evaluation of the cost performance of the SOFC cell in the market. Int J Hydrogen Energy 1996;21:129–35.
[13] Marocco P, Gandiglio M, Santarelli M. When SOFC-based cogeneration systems become convenient? A cost-optimal analysis. Energy Rep 2022;8:8709–21.
[14] Leone P, Santarelli M, Asinari P, Calì M, Borchiellini R. Experimental investigations of the microscopic features and polarization limiting factors of planar SOFCs with LSM and LSCF cathodes. J Power Sources 2008;177:111–22.
[15] Manenti F, Pelosato R, Vallevi P, Leon-Garzon AR, Dotelli G, Vita A, et al. Biogas-fed solid oxide fuel cell (SOFC) coupled to tri-reforming process: modelling and simulation. Int J Hydrogen Energy 2015;40:14640–50.
[16] De Lorenzo G, Corigliano O, Lo Faro M, Frontera P, Antonucci P, Zignani SC, et al. Thermoelectric characterization of an intermediate temperature solid oxide fuel cell system directly fed by dry biogas. Energy Convers Manag 2016;127:90–102.
[17] Yahya A, Ferrero D, Dhahri H, Leone P, Slimi K, Santarelli M. Electrochemical performance of solid oxide fuel cell: experimental study and calibrated model. Energy 2018;142:932–43.
[18] Del Zotto L, Tamburrano G, Dell'Era A, Hatunoglu A, Ciro E. Determination and validation of polarization losses parameters to predict current/voltage-characteristics for SOFC button cell. Energy Convers Manag 2024;299:117877.
[19] Yang T, Sezer H, Celik IB, Finklea HO, Gerdes K. Prediction of SOFC performance with or without experiments: a study on minimum requirements for experimental data. ECS Trans 2015;68:2397.
[20] Beale SB, Andersson M, Boigues-Muñoz C, Frandsen HL, Lin Z, McPhail SJ, et al. Continuum scale modelling and complementary experimentation of solid oxide cells. Prog Energy Combust Sci 2021;85:100902.
[21] Bilgili M, Görüryılmaz M. A 3D CFD modelling of different flow types for an anode supported hydrogen fed SOFC. 2017.
[22] Sezer H, Mason JH, Celik IB, Yang T. Three-dimensional modeling of performance degradation of planar SOFC with phosphine exposure. Int J Hydrogen Energy 2021;46:6803–16.
[23] Ferguson JR, Fiard JM, Herbin R. Three-dimensional numerical simulation for various geometries of solid oxide fuel cells. J Power Sources 1996;58:109–22.
[24] Mahcene H, Moussa HB, Bouguettaia H, Bechki D, Babay S, Meftah MS. Study of species, temperature distributions and the solid oxide fuel cells performance in a 2-D model. Int J Hydrogen Energy 2011;36:4244–52.
[25] Barzi YM, Raoufi A, Lari H. Performance analysis of a SOFC button cell using a CFD model. Int J Hydrogen Energy 2010;35:9468–78.
[26] Hussain J, Ali R, Akhtar MN, Jaffery MH, Shakir I, Raza R. Modeling and simulation of planar SOFC to study the electrochemical properties. Curr Appl Phys 2020;20:660–72.
[27] Cheddie DF, Munroe NDH. A dynamic 1D model of a solid oxide fuel cell for real time simulation. J Power Sources 2007;171:634–43.
[28] Karcz M. From 0D to 1D modeling of tubular solid oxide fuel cell. Energy Convers Manag 2009;50:2307–15.
[29] Daneshvar K, Dotelli G, Cristiani C, Pelosato R, Santarelli M. Modeling and parametric study of a single solid oxide fuel cell by finite element method. Fuel Cell 2014;14:189–99.
[30] Celik AN. Three-dimensional multiphysics model of a planar solid oxide fuel cell using computational fluid dynamics approach. Int J Hydrogen Energy 2018;43:19730–48.
[31] Machaj K, Kupecki J, Niemczyk A, Malecha Z, Brouwer J, Porwisiak D. Numerical analysis of the relation between the porosity of the fuel electrode support and functional layer, and performance of solid oxide fuel cells using computational fluid dynamics. Int J Hydrogen Energy 2024;52:936–51.
[32] Yang T, Sezer H, Celik I, Finklea H, Gerdes K. Prediction of SOFC performance with or without experiments: a study on minimum requirements for experimental data. 2015.
[33] Campanari S, Iora P. Definition and sensitivity analysis of a finite volume SOFC model for a tubular cell geometry. J Power Sources 2004;132:113–26.
[34] Campanari S, Iora P. Comparison of finite volume SOFC models for the simulation of a planar cell geometry. Fuel Cell 2005;5:34–51.
[35] Peksen M. A coupled 3D thermofluid–thermomechanical analysis of a planar type production scale SOFC stack. Int J Hydrogen Energy 2011;36:11914–28.
[36] Li A, Song C, Lin Z. A multiphysics fully coupled modeling tool for the design and operation analysis of planar solid oxide fuel cell stacks. Appl Energy 2017;190:1234–44.
[37] Xiong X, Liang K, Ma G, Ba L. Three-dimensional multi-physics modelling and structural optimization of SOFC large-scale stack and stack tower. Int J Hydrogen Energy 2023;48:2742–61.
[38] Chan SH, Khor KA, Xia ZT. A complete polarization model of a solid oxide fuel cell and its sensitivity to the change of cell component thickness. J Power Sources 2001;93:130–40.
[39] Noren DA, Hoffman MA. Clarifying the Butler–Volmer equation and related approximations for calculating activation losses in solid oxide fuel cell models. J Power Sources 2005;152:175–81.
[40] Andersson M, Yuan J, Sundén B. SOFC cell design optimization using the finite element method based CFD approach. Fuel Cell 2014;14:177–88.
[41] Goodwin DG, Zhu H, Colclasure AM, Kee RJ. Modeling electrochemical oxidation of hydrogen on Ni–YSZ pattern anodes. J Electrochem Soc 2009;156:B1004.
[42] Ferrero D, Lanzini A, Santarelli M. Solid oxide fuel cells modeling. 2017. p. 291–342.
[43] John BB. Mass transfer in heterogeneous catalysis, C. N. Satterfieldvol. 16. Cambridge, Mass: Massachusetts Institute of Technology Press; 1970. p. 509–10 (1970). 267 pages. Aiche Journal.
[44] Hines. Mass transfer : fundamentals and application/by Anthony L. Hines and Robert N. Maddox. Prentice-Hall1985.
[45] Poling BE, Prausnitz JM, O'Connell JP. Properties of gases and liquids. fifth ed. ed. New York: McGraw-Hill Education; 2001.
[46] P.D. Neufeld, A.R. Janzen, R.A. Aziz. Empirical equations to calculate 16 of the transport collision integrals Ω(l,. s) * for the Lennard-Jones (12–6) Potential. J Chem Phys 2003;57:1100–2.
[47] Lehnert W, Meusinger J, Thom F. Modeling of gas transport phenomena in SOFC anodes. J Power Sources 2000;87:57–63.
[48] Fuller EN, Schettler PD, Giddings JC. New method for prediction of binary gas-phase diffusion coefficients. Ind Eng Chem 1966;58:18–27.
[49] Pollard WG, Present RD. On gaseous self-diffusion in long capillary tubes. Phys Rev 1948;73:762–74.
[50] Veldsink JW, van Damme RMJ, Versteeg GF, van Swaaij WPM. The use of the dusty-gas model for the description of mass transport with chemical reaction in porous media. Chem Eng J Biochem Eng J 1995;57:115–25.
[51] Krishna R, van Baten JM. Investigating the validity of the Bosanquet formula for estimation of diffusivities in mesopores. Chem Eng Sci 2012;69:684–8.
[52] Chan SH, Xia Z. Polarization effects in electrolyte/electrode-supported solid oxide fuel cells. J Appl Electrochem 2002;32:339–47.
[53] Ni M, Leung MKH, Leung DYC. Parametric study of solid oxide fuel cell performance. Energy Convers Manag 2007;48:1525–35.
[54] Kim J-W, Virkar AV, Fung K-Z, Mehta K, Singhal SC. Polarization effects in intermediate temperature, anode-supported solid oxide fuel cells. J Electrochem Soc 1999;146:69–78.
[55] Lesaja G. Introducing interior-point methods for introductory operations research courses and/or linear programming courses. Open Oper Res J 2009;3:1–12.
[56] Magar HS, Hassan RYA, Mulchandani A. Electrochemical impedance spectroscopy (EIS): principles, construction, and biosensing applications. Sensors 2021;21:6578.
[57] Ebrahimi M. 13 - fuel cell power plants. In: Ebrahimi M, editor. Power generation technologies. Academic Press; 2023. p. 533–74.
[58] Mai A, Haanappel VAC, Uhlenbruck S, Tietz F, Stöver D. Ferrite-based perovskites as cathode materials for anode-supported solid oxide fuel cells: Part I. Variation of composition. Solid State Ionics 2005;176:1341–50.
[59] Hansen KK. A-site deficient (Pr0.6Sr0.4) 1 − s Fe0.8Co0.2O3 − δ perovskites as solid oxide fuel cell cathodes. J Electrochem Soc 2009;156:B1257–60.
[60] Nikonov AV, Kuterbekov K, Bekmyrza KZ, Pavzderin NB. A brief review of conductivity and thermal expansion of perovskite-related oxides for SOFC cathode. Eurasian J Phys Function Mater 2018;2:274–92.
[61] Steele BCH. Appraisal of Ce1−yGdyO2−y/2 electrolytes for IT-SOFC operation at 500°C. Solid State Ionics 2000;129:95–110.
[62] Lo Faro M, Vecino-Mantilla S. High-entropy proton conductive electrolyte for intermediate temperature operation. ECS Trans 2023;111:1817.
[63] Noponen M, Torri P, Göös J, Chade D, Hallanoro P, Temmo A, et al. Status of solid oxide fuel cell development at Elcogen. ECS Trans 2015;1:151–6. ed.
[64] Bertoldi M, Bucheli O, Ravagni AV. Development, manufacturing and deployment of SOFC-based products at SOLIDpower. ECS Trans 2017;1:117–23. ed.
[65] Tao S, Irvine JTS. A redox-stable efficient anode for solid-oxide fuel cells. Nat Mater 2003;2:320–3.
[66] Vecino-Mantilla S, Zignani SC, Vannier R-N, Aricò AS, Lo Faro M. Insights on a Ruddlesden-Popper phase as an active layer for a solid oxide fuel cell fed with dry biogas. Renew Energy 2022;192:784–92.
[67] Lo Faro M, Campagna Zignani S, Aricò AS. Lanthanum ferrites-based exsolved perovskites as fuel-flexible anode for solid oxide fuel cells. Materials 2020;13.
[68] Ni M, Leung MKH, Leung DYC. Micro-scale modelling of solid oxide fuel cells with micro-structurally graded electrodes. J Power Sources 2007;168:369–78.

[69] Campana R, Larrea A, Merino RI, Villareal I, Orera VM. SOFC mini-tubulares basadas en YSZ. Boletin de la Sociedad Espanola de Ceramica y Vidrio 2008;47:189–95.
[70] García-Camprubí M, Izquierdo S, Fueyo N. Challenges in the electrochemical modelling of solid oxide fuel and electrolyser cells. Renew Sustain Energy Rev 2014;33:701–18.
[71] Kawashima T, Hishinuma M. Analysis of electrical conduction paths in Ni/YSZ particulate composites using percolation theory. Mater Trans, JIM 1996;37:1397–403.
[72] Anselmi-Tamburini U, Chiodelli G, Arimondi M, Maglia F, Spinolo G, Munir ZA. Electrical properties of Ni/YSZ cermets obtained through combustion synthesis. Solid State Ionics 1998;110:35–43.
[73] Zhang X, Wang L, Espinoza M, Li T, Andersson M. Numerical simulation of solid oxide fuel cells comparing different electrochemical kinetics. Int J Energy Res 2021;45:12980–95.
[74] Ighodaro O, Scott K, Xing L. An isothermal study of the electrochemical performance of intermediate temperature solid oxide fuel cells. J Power Energy Eng 2017;5:97–122.
[75] Pianko-Oprych P, Palus M. Simulation of SOFCs based power generation system using Aspen. Pol J Chem Technol 2017;19.
[76] Cayan FN, Pakalapati SR, Elizalde-Blancas F, Celik I. On modeling multi-component diffusion inside the porous anode of solid oxide fuel cells using Fick's model. J Power Sources 2009;192:467–74.
[77] Blum L, Batfalsky P, Fang Q, De Haart LGJ, Malzbender J, Margaritis N, et al. Solid oxide fuel cell, stack and system development status at Forschungszentrum Jülich. ECS Trans 2015;1:157–69. ed.
[78] Yokokawa H. Current status of rapid evaluation of durability of six SOFC stacks within NEDO project. ECS Trans 2015;1:1827–36. ed.
[79] Aguilo-Rullan A, Atanasiu M, Biebuyck B, Lymperopoulos N, Marenco C, Tsimis D. The status of SOFC and SOEC R&D in the European fuel cell and hydrogen joint undertaking programme. ECS Trans 2017;1:41–61. ed.
[80] Nirasawa H. Current status of national SOFC projects in Japan. ECS Trans 2017;1:33–40. ed.
[81] Cassidy M. Trends in the processing and manufacture of solid oxide fuel cells. Wiley Interdisc Rev: Energy Environ 2017;6.